Bulletin of the Seismological Society of America, Vol. 101, No. 5, pp. 2388–2398, October 2011, doi: 10.1785/0120100318

Coda-Derived Source Parameters of Earthquakes and Their Scaling Relationships in the Korean Peninsula

by Seung-Hoon Yoo,* Junkee Rhie, Hoseon Choi,† and Kevin Mayeda‡

Abstract We applied the coda-derived source spectrum method of Mayeda *et al.* (2003) to earthquakes in and around the Korean peninsula. After empirical calibrations, we derived source spectra of the earthquakes. From the coda-derived spectra, we estimated valuable source parameters such as the seismic moment, corner frequency, and radiated energy for small events with $M_w < 3.5$. We derived simple linear relationships between the coda spectral amplitudes and local magnitudes reported from the Korea Meteorological Administration and Korea Institute of Geoscience and Mineral Resources. These relationships can be used to estimate stable local magnitudes for future earthquakes using a small number of stations. To investigate whether the earthquakes occurring in this region obey self-similarity, we examined the scaling relationships between dynamic and static source parameters, such as the corner frequency, radiated energy, and scaled energy versus seismic moment. The scaling relationship between the corner frequency and seismic moment showed clear nonself-similarity with a scaling parameter of 0.54; this value is more or less consistent with previous results for different regions. Scaling relations of radiated energy and scaled energy versus the seismic moment also show size-dependent behavior that cannot be explained by self-similarity; this result implies that the rupture dynamics of small and large earthquakes are different in this region. Our observation provides further evidence supporting the nonself-similarity of earthquakes.

Introduction

The source spectra of earthquakes contain important information on the earthquake source processes, namely the seismic moment (M_0), corner frequency (f_c), and radiated seismic energy (E_R), which can all be easily measured from a well-determined source spectrum. The direct phases of the earthquake have historically been used to derive the source spectrum (e.g., Prieto *et al.*, 2004; Izutani, 2005; Venkataraman *et al.*, 2006). However, a reliable source spectrum is difficult to obtain from the direct phases in most cases because the amplitudes of the direct phases recorded at different stations vary significantly due to the source radiation pattern, source directivity, site conditions, and heterogeneities along the propagation path. Although multistation averaging can reduce the variability of the direct wave-amplitude measurements, it is still difficult to properly account for all factors affecting the amplitudes. To circumvent this problem, methods have been developed that use coda waves instead of direct phases (e.g., Mayeda and Walter, 1996) because coda waves can inherently average out unwanted path, site, and source variability (Aki and Chouet, 1975; Rautian and Khalturin, 1978). Several previous studies have shown that coda measurements are 3–4 times more stable than direct wave measurements (e.g., Mayeda *et al.*, 2007; Mayeda and Malagnini, 2010). Stable coda amplitude measurements have been used to study the magnitudes of local and regional earthquakes (e.g., Mayeda and Walter, 1996; Mayeda *et al.*, 2003; Morasca *et al.*, 2005; Mayeda *et al.*, 2005), site effects (e.g., Malagnini *et al.*, 2004), seismic discrimination of underground nuclear explosions (e.g., Murphy *et al.*, 2009), regional attenuation structures (e.g., Zolezzi *et al.*, 2008; Morasca *et al.*, 2008), and dynamic source scaling (e.g., Mayeda and Malagnini, 2009; Yoo *et al.*, 2010).

The coda amplitudes can be measured from consecutive narrowband coda envelopes. After correcting the coda envelope measurements for path, site, and S-to-coda transfer functions, we can reconstruct the source spectrum of the earthquake. Several previous results obtained from the coda-based method for different regions showed that empirical correc-

*Now at Berkeley Seismological Laboratory, University of California, Berkeley California 94720-4760.

†Also at School of Earth and Environmental Sciences, Seoul National University, Seoul 151-742, South Korea.

‡Also at Weston Geophysical Corporation, 181 Beford St., Ste.1, Lexington, Massachusetts 02420.

tions for those factors can provide stable and reliable source spectra (e.g., Mayeda *et al.*, 2003; Morasca *et al.*, 2005).

In this study, we applied the coda-based method to derive *S*-wave source spectra of earthquakes occurring in the Korean peninsula and surrounding regions. From the derived source spectrum, we measured the seismic moment, corner frequency, and radiated energy of the earthquakes. In addition, we investigated the scaling relations of several parameters (such as the corner frequency, radiated energy, and scaled energy) versus the seismic moment. The measurements of the seismic moment are important for completing the earthquake catalog and also provide useful information for evaluating seismic hazards in a region. The scaling relations are important for resolving whether the earthquakes obey self-similarity or not. Self-similarity implies that large and small earthquakes involve the same physical mechanism (Kanamori and Anderson, 1975), whereas nonself-similarity implies that the physical mechanism is size dependent. Although several studies have been conducted with the aim of resolving the problem by using various approaches (e.g., Kanamori *et al.*, 1993; Singh and Ordaz, 1994; Abercrombie, 1995; Choy and Boatwright, 1995; Mayeda and Walter, 1996; McGarr, 1999; Ide and Beroza, 2001; Izutani and Kanamori, 2001; Ide *et al.*, 2003; Kanamori and Rivera, 2004; Prieto *et al.*, 2004; Izutani, 2005; Mayeda *et al.*, 2007), a conclusive answer is still far from being established. However, many recent studies using the stable coda-based approaches have reported supporting evidence for the nonself-similarity of earthquakes; our results also demonstrate that the earthquakes that occurred in the study area followed nonself-similarity.

Data and Methods

We analyzed 392 earthquakes ($1.5 < M_L < 6.5$) that occurred in and around the Korean Peninsula for the seven-year period of 2001–2007 (Fig. 1a). Broadband waveforms (100 samples/s) recorded by 17 seismic stations (16 STS-2 and 1 CMG-3TB seismometers) operated by the Korea Institute of Geoscience and Mineral Resources (KIGAM) and Korea Meteorological Administration (KMA) were used (see Fig. 1a). KIGAM and KMA routinely report the origin time, epicenter, and network-averaged local magnitude (M_L). The origin times and event locations are necessary for further analysis, and those parameters were basically taken from the KIGAM catalog. However, the KMA catalog was also used for some events that were not listed in the KIGAM catalog.

In this study, the coda-derived source spectrum method (e.g., Mayeda and Walter, 1996; Mayeda *et al.*, 2003; Morasca *et al.*, 2005) was applied to investigate source parameters of the earthquakes and their scaling relations. We mainly followed the procedure developed by Mayeda *et al.* (2003).

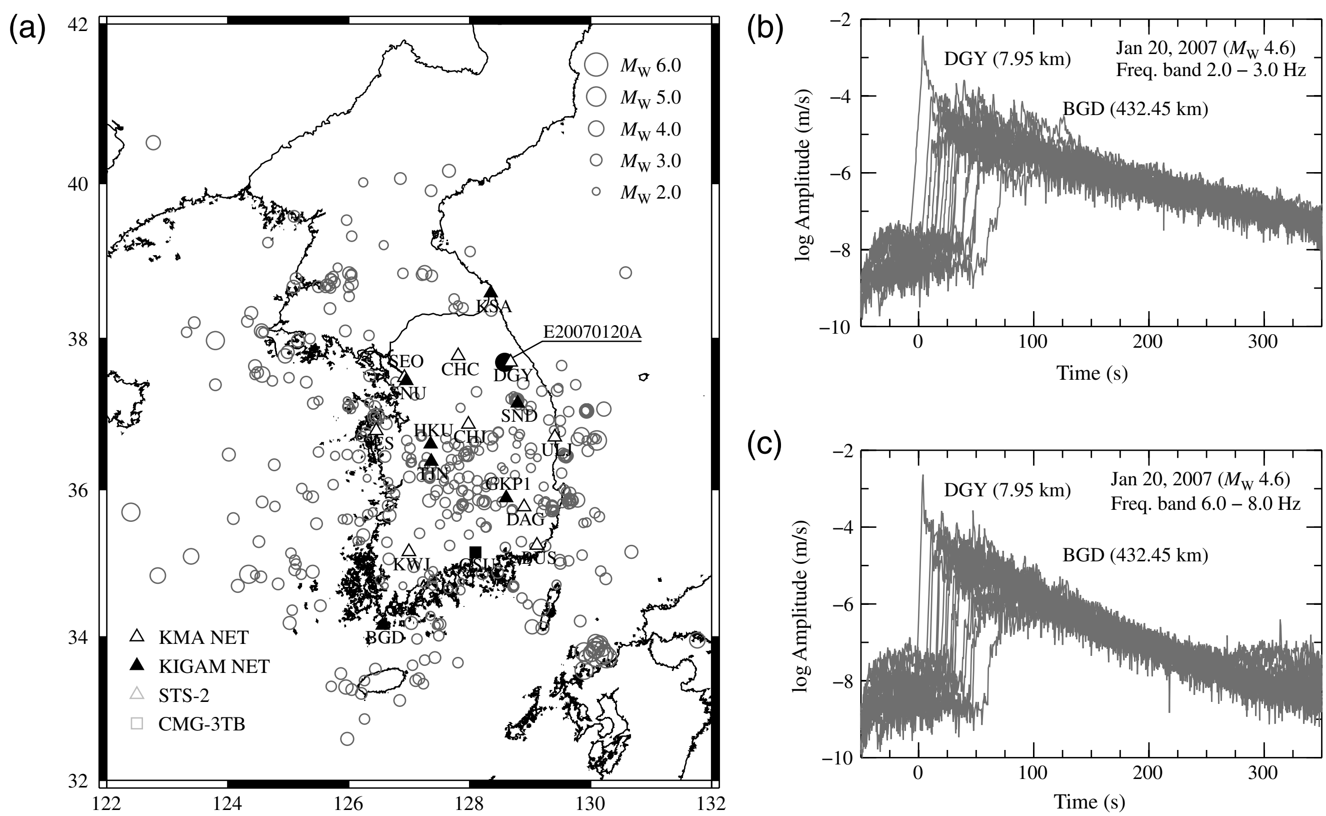

Figure 1. (a) Location map of the 392 events and 17 broadband stations used in this study. Symbol size is proportional to the coda-derived moment magnitude of event. (b) Example of selected narrowband envelopes of the 20 January 2007 event [black solid circle in (a)] for the 2.0–3.0 Hz band. (c) Same as (b) but for the 6.0–8.0 Hz band.

To compute consecutive narrowband coda envelopes for velocity seismograms in m/s, we removed the instrument response from two horizontal components and then applied an eighth-order and zero phase (four poles and two passes) Butterworth filter for 16 narrow frequency bands ranging between 0.05 and 25 Hz (see Table 1). The instrument responses of the STS-2 and CMG-3TB sensors are flat over the given frequency range, and the mean was removed before band-pass filtering. For each frequency band, the narrowband envelope was computed from the band-pass-filtered waveform and its Hilbert transform. We then took $\log_{10}$ of both horizontal envelopes and averaged them. In this step, we removed data if the difference in the peak amplitudes of both horizontal components was larger than 20%. After smoothing with a moving window, we obtained the final narrowband envelope for each event–station pair. Figure 1b shows the coda envelopes recorded at selected stations for the 20 January 2007 event (M_w 4.6) at 2.0–3.0 and 6.0–8.0-Hz bands. The peak amplitudes associated with direct *S* or *Lg* phases clearly vary significantly for different stations. On the other hand, the levels of the coda envelopes at the latter part are almost identical. As found in other studies (e.g., Mayeda *et al.*, 2007; Mayeda and Malagnini, 2010), this confirms that the coda waves are less sensitive to the source radiation, path, and site effects than are direct *S* or *Lg* waves.

To measure the dimensionless coda amplitude from the observed coda envelopes, we need a reference envelope for each frequency band. In this study, we used a simple functional form introduced by Mayeda *et al* (2003). This form was developed based on the single-scattering model of Aki (1969). However, the distance-dependent coda envelope shape was fit empirically. Mayeda *et al.* (2003) demonstrated that this form reasonably fits the shapes of both local and regional coda envelopes. The observed coda envelope at a given center frequency f and distance r can be modeled by

$$A_C(t,f,r) = W_0(f)S(f)P(f,r)E(t,f,r), \quad (1)$$

where $W_0(f)$ is the *S*-wave source amplitude, $S(f)$ is the term that includes both the site response and the *S*-to-coda transfer function resulting from scattering, $P(f,r)$ is the term including the effects of geometrical spreading and attenuation (both scattering and absorption), and $E(t,f,r)$ is an empirical synthetic envelope representing the coda envelope shape. The units of $A_C(t,f,r)$, $W_0(f)$, $S(f)$, $E(t,f,r)$, and $P(f,r)$ are m/s, dyn·cm, 1/(dyn·cm), m/s, and dimensionless, respectively. $E(t,f,r)$ can be defined by

$$E(t,f,r) = H\left(t - \frac{r}{v(f,r)}\right)\left(t - \frac{r}{v(f,r)}\right)^{-\gamma(f,r)} \times \exp\left[b(f,r)\left(t - \frac{r}{v(f,r)}\right)\right], \quad (2)$$

where H is the Heaviside step function, t is the time elapsed from the event origin time in seconds, $v(f,r)$ is the velocity of the peak arrival in km/s, and parameters $\gamma(f,r)$ and $b(f,r)$ control the shape of the coda envelope. The coda shape parameters γ and b represent the amplitude decay, which depends on the geometrical spreading and decay rate of the coda waves due to intrinsic absorption, respectively. γ controls the shape of the coda envelope immediately following the direct waves, whereas b controls the slope of the coda envelope in the latter part. Because $E(t,f,r)$ does not depend upon the size of the earthquake, we can use only high-quality data ($M_L > 3.0$) with a long-lasting coda and good signal-to-noise ratio for estimating $E(t,f,r)$. The estimated $E(t,f,r)$ was used to measure the dimensionless coda amplitude of all events, including small events that were not used for $E(t,f,r)$ calibration. To determine $E(t,f,r)$, we need to estimate $v(f,r)$, $b(f,r)$, and $\gamma(f,r)$. For each frequency and event-station pair, the velocity of the main peak can be measured in the observed coda envelope. This dataset

Table 1
Calibration Parameters for Peak Velocity and Coda Shape Parameters γ and b for 16 Narrowband Frequencies

	Peak Velocity (v)			Coda Shape Parameter γ			Coda Shape Parameter b		
Frequency (Hz)	v_0	v_1	v_2	γ_0	γ_1	γ_2	b_0	b_1	b_2
0.05–0.1	3.38	33.0	36.5	0.6	−40	1001	-1.470×10^{-4}	0.0	0
0.1–0.2	3.28	4.0	2.5	0.3	−20	31	-2.190×10^{-4}	0.0	0
0.2–0.3	3.32	14.5	8.0	0.3	−250	1001	-4.670×10^{-4}	0.1	200
0.3–0.5	3.40	31.5	17.0	0.3	−270	971	-1.115×10^{-3}	0.1	190
0.5–0.7	3.39	21.5	11.5	−0.2	−820	701	-1.740×10^{-3}	0.0	0
0.7–1.0	3.39	13.0	7.0	0.0	−330	331	-2.396×10^{-3}	0.0	0
1.0–1.5	3.39	11.0	6.0	0.2	−270	451	-3.160×10^{-3}	0.0	0
1.5–2.0	3.42	20.0	10.5	0.3	−140	331	-4.315×10^{-3}	0.0	0
2.0–3.0	3.42	14.5	8.0	0.3	−320	1001	-5.484×10^{-3}	0.0	0
3.0–4.0	3.44	15.5	8.0	0.0	−690	971	-6.927×10^{-3}	0.0	0
4.0–6.0	3.45	13.5	7.0	0.0	−620	991	-8.677×10^{-3}	0.0	0
6.0–8.0	3.47	17.0	9.0	−0.1	−640	971	-9.731×10^{-3}	0.3	190
8.0–10.0	3.46	16.5	8.5	−0.1	−700	1001	-1.155×10^{-2}	0.1	270
10.0–15.0	3.46	21.0	11.0	−0.1	−590	921	-1.300×10^{-2}	0.1	30
15.0–20.0	3.41	20.0	10.5	0.1	−100	181	-1.539×10^{-2}	0.2	160
20.0–25.0	3.38	23.5	12.5	0.1	−50	71	-1.162×10^{-2}	2.0	660

was used to estimate $v(f, r)$, which can be represented as a simple hyperbolic function:

$$v(f, r) = v_0(f) - \frac{v_1(f)}{v_2(f) + r}, \quad (3)$$

where v_0, v_1, and v_2 can be determined by finding the best matching $v(f, r)$ with the observed velocities using a grid search. A similar technique can be used for determining coda shape parameters γ and b. However, they cannot be measured directly from the observed envelope, as is done for the velocity of the main peak. In equations (1) and (2), we note that only $E(t, f, r)$ is time dependent, and it becomes infinite at the peak arrival time ($t = r/v$). Because other terms such as $W_0(f)$, $S(f)$, and $P(f, r)$ are time invariant, the amplitude decay rate after $t = r/v$ in the observed coda envelope depends completely on $E(t, f, r)$, regardless of the absolute value of the main peak. Therefore, we can find optimal coda shape parameters for each frequency and event–station pair by matching $E(t, f, r)$ with the observed decaying rate. Here, we calculated $E(t, f, r)$ from 1 second after the peak arrival to avoid a singularity. Then γ was estimated using a grid search ($0.1 \le \gamma \le 1.6$), and b was determined by least-square inversion after fixing γ. The functional forms of the coda shape parameters as a function of distance are also represented by hyperbolic forms,

$$\gamma(f, r) = \gamma_0(f) - \frac{\gamma_1(f)}{\gamma_2(f) + r} \quad (4)$$

and

$$b(f, r) = b_0(f) - \frac{b_1(f)}{b_2(f) + r}, \quad (5)$$

where γ_0, γ_1, γ_2, b_0, b_1, and b_2 can be found by the same technique used for $v(f, r)$. All parameters defining $v(f, r)$, $\gamma(f, r)$, and $b(f, r)$ are listed in Table 1.

Once $E(t, f, r)$ is defined, the dimensionless coda amplitude can be easily measured by a DC shift of $\log_{10} E(t, f, r)$ to match the observed coda envelope using an L1 norm. It indicates that the dimensionless coda amplitude is the difference of $A_C(t, f, r)$ and $E(t, f, r)$ in log units, which includes the $W_0(f)$, $P(f, r)$, and $S(f)$. Before measuring the dimensionless coda amplitude, a small amount of time shift was allowed to remove effects due to the possible misalignment of the observed and synthetic coda envelopes. In this step, the maximum length of the time window for the coda envelope was determined based on the signal-to-noise ratio and stability condition of measurement (Mayeda *et al.*, 2003). Figure 2 shows an example of the coda envelopes for the 20 January 2007 event at station SEO. The observed coda envelope clearly varies with different frequencies, and our simple empirical synthetic envelope fits the observation very well.

The final value we want to obtain is $W_0(f)$, which corresponds to the *S*-wave source amplitude at a given frequency. To get $W_0(f)$, we still need to correct for $S(f)$ and $P(f, r)$ in the measured dimensionless coda amplitude. The correction

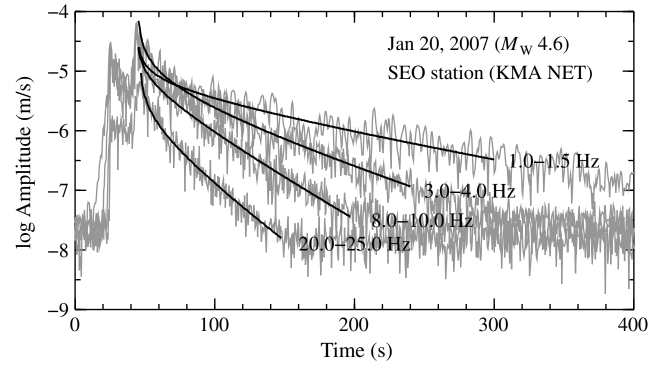

Figure 2. Comparison of narrowband coda envelopes (gray lines) and corresponding synthetics (black lines) at selected frequency bands.

for $P(f, r)$, which is known as the path correction, was performed using an empirical correction known as the extended Street and Herrmann (ESH) correction (Morasca *et al.*, 2008). The path-correction term can be separated into two subterms (e.g., Street*et al.*, 1975), such as geometrical spreading and scattering attenuation, and can be represented by

$$P(f, r) = G(r) \times \exp\left(-\frac{\pi f r}{v Q(f)}\right), \quad (6)$$

where v is the phase velocity, $Q(f)$ is the frequency-dependent attenuation coefficient, and $G(r)$ is the geometric spreading term. In the ESH correction, $G(r)$ is separately defined for three distance ranges of r:

$$G(r) = r^{-p_1}, \qquad r < R_1,$$
$$G(r) = R_1^{-p_1}(r/R_1)^{-[p_1+\Delta p(r)/2]} \qquad R_1 < r < R_2,$$
where $\Delta p(r) = \log(r/R_1)(p_2 - p_1)/\log(R_2/R_1)$,
$$G(r) = R_1^{-p_1}(R_2/R_1)^{-[p_1+\Delta p(r)/2]}(r/R_2)^{-p_2},$$
$$r > R_2,$$
where $\Delta p(r) = (p_2 - p_1)$. (7)

Here, $R_1 = R_C/F$ and $R_2 = R_C \times F$, where R_C is the critical distance and F is the transition factor (≥ 1). To define the path-correction term, we selected the dimensionless coda amplitude data for common events only if more than 12 observations were available. The basic idea of the empirical path-correction is to find the path-correction term that minimizes the scatter of the distance-corrected amplitudes for each event. For each frequency and event, we obtained p_1, R_C, F, and Q using the Powell search scheme (Powell, 1964). In this step, the long-distance spreading power p_2 was fixed to 0.5, and the phase velocity v was set to 3.5 km/s by assuming a surface wave–like geometrical spreading at long distances (e.g., Malagnini *et al.*, 2002; Ford *et al.*, 2008). Table 2 shows the resulting path-correction parameters for all frequency bands. Here, we note that the derived Q is just an empirical parameter and that it is different from the real scattering Q representing the scattering attenuation of the region. Figure 3 shows examples of path correction for the several events at the 2.0–3.0-Hz frequency band.

The final step of the calibration is to correct for $S(f)$ (hereafter referred to as the site correction), which includes the S-to-coda transfer function and the relative site effects. We used seven events ($M_w > 4.0$), including the mainshock of the 2005 Fukuoka sequence (M_w 6.6) and its largest aftershock (M_w 5.4), for the site correction. The waveforms from all events showed good signal-to-noise ratio for all frequency bands and were well recorded by all stations used in this study. For the site correction, predefined seismic moments are required, and they were obtained from a previous study (Rhie and Kim, 2010) and the F-net moment tensor catalog (see Data and Resources).

Because we have the seismic moments of the events, the theoretical source spectra, $W_0(f) = M_0/[1 + (f/f_c)^2]$, which has ω^{-2} spectral shape (Brune, 1970), can be calculated for the fixed apparent stress, scaling parameter ε, and reference seismic moment using the magnitude distance and amplitude correction algorithm, which allows for the variation of the corner frequency and apparent stress that does not have to be self-similar (Walter and Taylor, 2001). The corner frequency (f_c) and apparent stress (σ_a) can be defined as

$$f_c = \frac{1}{2\pi}(k\sigma_a/M_0)^{1/3},$$
$$\sigma_a = \sigma'_a(M_0/M'_0)^{\varepsilon/(\varepsilon+3)} \quad \text{and}$$
$$k = 16\pi\Big/\left[\beta_S^2\left(\frac{R_{\theta\phi P}^2\zeta^2}{\alpha_S^5} + \frac{R_{\theta\phi S}^2}{\beta_S^5}\right)\right], \tag{8}$$

where σ'_a and M'_0 are the apparent stress and seismic moment of the reference event, ε represents the deviation from self-similarity and should be a small positive number (Kanamori and Rivera, 2004), k is a constant related to the P- and S-wave velocities at the source (α_S and β_S), $R_{\theta\phi P}$ and $R_{\theta\phi S}$ are the radiation pattern coefficients of P and S waves, and ζ is the scale factor of the P- and S-wave corner frequencies. Here we used values of $R_{\theta\phi P} = 0.44$; $R_{\theta\phi S} = 0.60$ from Taylor *et al.* (2002); $\zeta = 1$ from Walter and Taylor (2001); and $\alpha_S = 6000$ and $\beta_S = 3500$ in m/s. In this step, any reference seismic moment can be used for the computation, and we selected $M'_0 = 4.0 \times 10^{23}$ dyn · cm($M_w \sim 5.0$). An arbitrary $S(f)$ can be derived by simultaneous DC shifting of the path-corrected amplitudes to match the theoretical source spectra of all reference events at each frequency. The best $S(f)$ can be obtained by finding the apparent stress and scaling parameter that maximize the variance reduction between the theoretical and calibrated spectra for all reference events and frequencies. Our grid-search results showed a clear maximum at an apparent stress of 0.91 MPa and scaling parameter of 0.0 (Fig. 4a). Tables 3 and 4 contain the parameters of $S(f)$ for all stations derived by the grid-search scheme. The variation in parameters for different stations represents the relative site amplification.

Results and Discussions

The coda-derived source spectra for all events at each station can be simultaneously calculated by tying the path-corrected coda amplitude to an absolute scale using the S-to-coda transfer function and relative site effects. The final coda-derived source spectrum for each event was estimated by averaging source spectra measured at all available stations. By doing this, we can make the source spectrum measurements more stable and enhance the reliability of the results. Because we assumed that the source spectrum can be represented by $W_0(f) = M_0/[1 + (f/f_c)^2]$, the seismic moment and corner frequency of the event can be estimated by finding the best-fitting theoretical spectrum using a grid search over M_0 and f_c. For small events, the corner frequency cannot be constrained by the method described previously in this paper. Therefore, we determined the corner frequencies only for events with $M_w > 2.0$. In contrast,

Table 2
Path-Correction Parameters for 16 Narrowband Frequencies

Frequency (Hz)	p_1	Critical Distance R_C	Transition Factor F	Derived Q
0.05–0.1	0.01337	219.09174	100.98828	468.03345
0.1–0.2	0.03811	220.56635	100.99976	999.96594
0.2–0.3	0.00000	97.39362	30.28028	679.89978
0.3–0.5	0.00000	175.24126	60.76254	534.94208
0.5–0.7	0.00000	103.67843	11.62897	782.71094
0.7–1.0	0.00874	400.60110	100.99876	1000.05212
1.0–1.5	0.00669	213.78596	99.54657	724.76160
1.5–2.0	0.00023	258.97458	71.65430	757.16943
2.0–3.0	0.04680	562.35828	66.62981	685.72040
3.0–4.0	0.11647	999.87537	2.58334	681.07129
4.0–6.0	0.00000	83.24528	3.51602	954.84796
6.0–8.0	0.05662	295.40558	101.00192	1000.41565
8.0–10.0	0.10407	633.21033	1.00008	1000.54419
10.0–15.0	0.00000	660.85693	1.00150	1005.82843
15.0–20.0	0.00000	589.45587	1.01173	1008.18011
20.0–25.0	0.00000	534.58392	1.00210	1008.69666

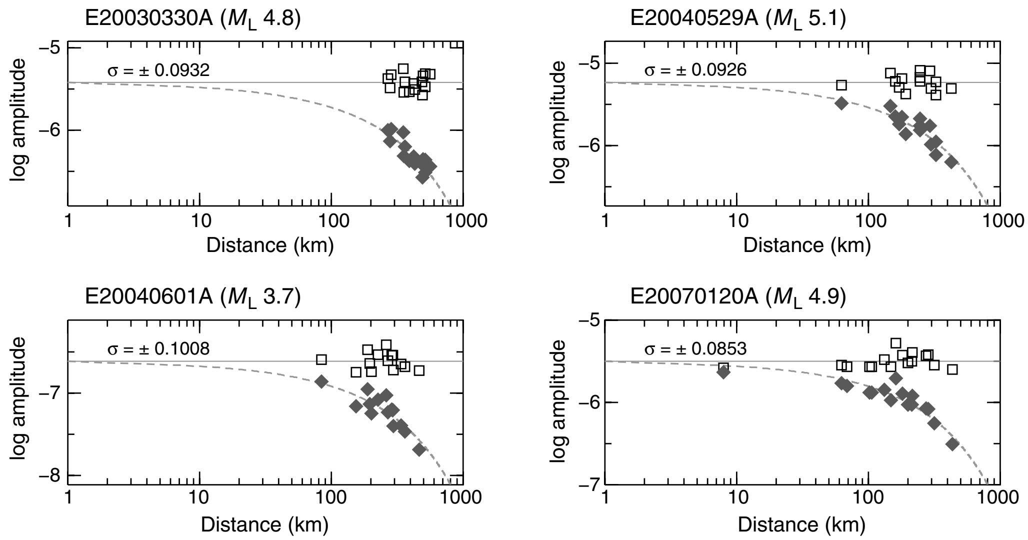

Figure 3. Best path-correction curves at 2.0–3.0 Hz (dotted curve) for selected events. Solid diamonds and open squares represent uncorrected and corrected amplitudes, respectively.

the seismic moment is generally sensitive to lower-frequency spectral amplitudes, and we can measure them for all events.

The seismic moment and thus moment magnitudes (Hanks and Kanamori, 1979) of all events considered in this study were determined (see Fig. 1a). About 89% (348 out of 392) of the events were less than M_w 3.5, which is too small for applying the traditional waveform inversion technique. Figure 5a shows the comparison of the selected coda-derived

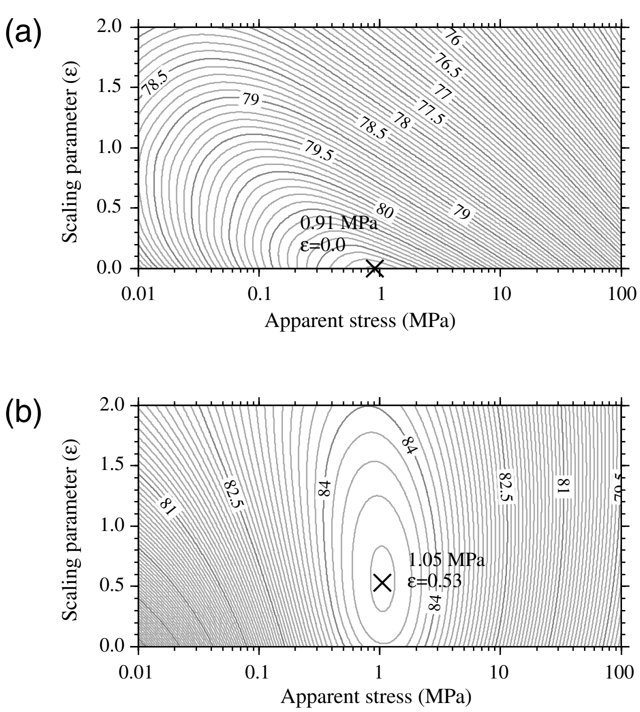

Figure 4. (a) Grid-search results for apparent stress and scaling parameter using seven events with $M_w > 4.0$. Cross indicates the point with maximum variance reduction. (b) Same as (a) for events with $M_w > 2.0$.

source spectra and their corresponding theoretical source spectra. To verify our seismic moment measurements, we compared the coda-derived moment magnitudes and those obtained from waveform inversion (e.g., Rhie and Kim, 2010). The comparison result shows that the root mean square (rms) error was only about 0.1 on the M_w scale between two magnitudes obtained from different datasets (Fig. 5b).

The moment magnitude may be the best way to represent the size of an earthquake because, in theory, it is not saturated and also has a clear physical meaning. However, other magnitude scales such as M_L, m_b, and M_S have their own advantages. In particular, the local magnitude (M_L) can depict damage due to an earthquake better than moment magnitude because the former depends strictly on the peak amplitude at a certain frequency (~1 Hz) that largely controls the structural damage. To estimate the coda-derived M_L, we developed a simple linear relation between the calibrated coda spectral amplitudes at certain frequencies and the M_L of the events. Two separate linear relations for network-averaged M_L catalogs published by KMA and KIGAM were obtained as follows:

$$M_{L(coda)} = 1.02488 \times \log_{10} A_{coda} - 18.2917 \quad \text{(for KMA)}$$
$$M_{L(coda)} = 0.92239 \times \log_{10} A_{coda} - 16.0216 \quad \text{(for KIGAM)} \tag{9}$$

where A_{coda} is the spectral amplitude at the 2.0–3.0-Hz band in dyn cm and $M_{L(coda)}$ denotes a coda-derived M_L (Fig. 6). Although Figure 6 shows the results for KMA, the results for KIGAM show similar features. The standard deviations of the difference in M_L between the network-averaged M_L and $M_{L(coda)}$ obtained from both relations were only about 0.15; the small standard deviations indicate that we can estimate the corresponding network-averaged M_L for future earthquakes by using the derived relations. However, we note that

Table 3
Site and *S*-to-Coda Correction Parameters [$\log_{10} S(f)$] for KMA Network Stations

Frequency (Hz)	KWJ	DGY	DAG	BUS	SES	SEO	ULJ	CHC	CHJ
0.05–0.1	30.02823	30.00864	29.98222	30.04961	30.03468	30.06380	29.94613	30.02767	30.01006
0.1–0.2	29.21919	29.16546	29.16697	29.15513	29.10974	29.21628	29.11982	29.15218	29.22771
0.2–0.3	29.06297	28.97083	29.00046	29.02176	29.02834	29.02765	28.92588	29.01833	29.04368
0.3–0.5	28.77337	28.76472	28.73485	28.70856	28.76780	28.78032	28.67180	28.72212	28.80106
0.5–0.7	28.74457	28.73231	28.64996	28.65845	28.70134	28.73596	28.71896	28.61990	28.77334
0.7–1.0	28.62304	28.55101	28.43597	28.56588	28.52812	28.55958	28.63808	28.48883	28.57618
1.0–1.5	28.28227	28.26824	28.12030	28.21866	28.25876	28.24557	28.29706	28.14686	28.30637
1.5–2.0	28.27606	28.22396	28.04688	28.14968	28.21516	28.20162	28.24688	28.13849	28.27797
2.0–3.0	27.90293	27.94533	27.73703	27.77524	27.85691	27.93357	27.87848	27.83751	27.95632
3.0–4.0	27.71758	27.78124	27.57521	27.66589	27.65072	27.71436	27.69695	27.56853	27.74383
4.0–6.0	27.49667	27.70609	27.39316	27.62632	27.48554	27.59126	27.62557	27.36369	27.57724
6.0–8.0	27.22023	27.41896	27.14084	27.34986	27.19831	27.26195	27.41198	27.10961	27.33146
8.0–10.0	27.17003	27.35895	27.19838	27.33990	27.17527	27.27352	27.48915	27.11116	27.32237
10.0–15.0	26.86123	27.01794	26.99983	27.08585	26.86756	27.07495	27.34191	26.84515	27.01728
15.0–20.0	26.71308	26.76868	26.71165	26.94095	26.43155	26.80499	26.84713	26.48603	26.65692
20.0–25.0	26.20149	26.37261	26.51450	26.60291	26.02015	26.38821	26.46235	26.24849	26.39503

the small standard deviations do not guarantee that the absolute values of $M_{L(coda)}$ are more reliable than the network-averaged M_L. The reliability of $M_{L(coda)}$ completely depends on the quality of the network M_L catalog. Two M_L catalogs used in this study showed considerable discrepancies for events they both catalogued. This indicates that a more stable and reliable network-averaged M_L catalog is necessary in this region. However, we do not discuss this issue further because it is beyond the scope of this study. Although the reliability does not increase, the advantage of the coda method is that a much smaller number of stations is required to achieve the same stability as the network M_L estimation. Therefore, we numerically tested whether we can estimate the network M_L using the coda waves recorded at only one station. We divided our dataset into two groups for different recording periods (2001–2006 and 2007). We derived the same linear relations presented previously in this paper, using only the dataset for 2001–2006 and then estimated $M_{L(coda)}$ for events occurring in 2007. The results show that predicted $M_{L(coda)}$ is consistent with the reported network-averaged M_L and that the maximum standard deviations for the stations are quite small ($\sigma_{max} < 0.10$).

Another important parameter that can be measured from the coda-derived source spectrum is the radiated energy (E_R). E_R represents the energy radiated through seismic waves during the earthquake process and can be defined as a summation of the *P*-wave radiated energy (E_P) and *S*-wave radiated energy (E_S). E_S can be calculated by

$$E_S = \frac{I}{4\pi^2 \rho \beta^5} \int_0^\infty |\omega \dot{M}(\omega)|^2 d\omega, \tag{10}$$

where $\dot{M}(\omega)$ is the coda-derived source spectrum and I is the rms radiation pattern of the *S* wave (e.g., Mayeda and Walter, 1996; Izutani and Kanamori, 2001); it is set to $2/5$. The density (ρ) and *S*-wave velocity (β) at the source depth were

Table 4
Site and *S*-to-Coda Correction Parameters [$\log_{10} S(f)$] for KIGAM Network Stations

Frequency (Hz)	TJN	GKP1	SNU	BGD	KSA	HKU	SND	GSU
0.05 – 0.1	30.07822	30.08974	29.99058	30.06128	29.85226	29.98987	29.94449	30.07314
0.1– 0.2	29.23617	29.19090	29.11166	29.21388	29.14060	29.18567	29.18598	29.20884
0.2 – 0.3	29.01586	29.06399	28.99153	29.10882	29.06873	29.08731	29.09927	28.95837
0.3 – 0.5	28.79984	28.76340	28.75475	28.81723	28.82018	28.74208	28.81124	28.70506
0.5 – 0.7	28.76336	28.71311	28.65061	28.73720	28.78949	28.65646	28.79235	28.63965
0.7 – 1.0	28.63733	28.56244	28.51686	28.66163	28.78150	28.52036	28.67654	28.52990
1.0 – 1.5	28.29086	28.24059	28.26865	28.32595	28.47139	28.19478	28.36748	28.15752
1.5 – 2.0	28.20103	28.19811	28.18373	28.37105	28.53363	28.09502	28.32610	28.13117
2.0 – 3.0	27.86823	27.88284	27.77467	28.05165	28.15746	27.71091	28.16827	27.83712
3.0 – 4.0	27.72424	27.66203	27.59814	27.82795	28.01783	27.46190	28.00746	27.66854
4.0 – 6.0	27.61360	27.45472	27.46904	27.66208	27.82452	27.24308	27.76356	27.60309
6.0 – 8.0	27.42009	27.17418	27.17386	27.38979	27.38475	27.08139	27.55592	27.45200
8.0 – 10.0	27.36495	27.13193	27.27807	27.32221	27.05732	27.08237	27.64400	27.54553
10.0 – 15.0	27.11527	26.80442	26.79598	27.01261	26.94363	26.93993	27.55232	27.26078
15.0 – 20.0	26.81731	26.54340	26.82323	26.61877	26.84874	26.75215	27.05224	26.96216
20.0 – 25.0	26.33688	26.30730	26.60246	25.95133	26.65960	26.57983	27.13948	26.78793

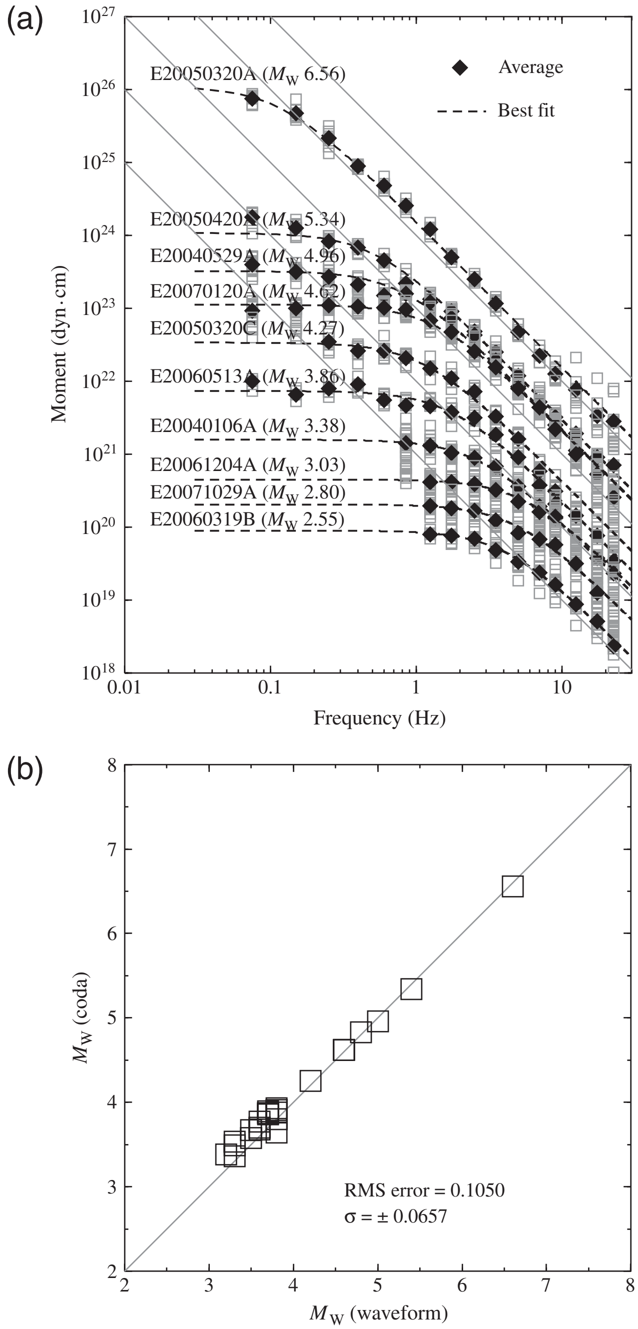

Figure 5. (a) Coda-derived source spectra of the selected events. Gray squares and black solid diamonds represent the spectral amplitudes of available stations and their average, respectively. The black dotted line indicates the best-fitting Brune spectra. For reference, omega-square fall-offs are indicated with gray lines. (b) Comparison between M_w (coda) and M_w (waveform). The small standard deviation indicates that the results are consistent with each other.

taken as 2700 kg/m^3 and 3.5 km/s, respectively. The limited frequency band used for calculating the energy can produce incorrect measurements (Ide and Beroza, 2001). Therefore, we compensated for the radiated energy outside of the frequency band considered (e.g., Mayeda and Walter, 1996).

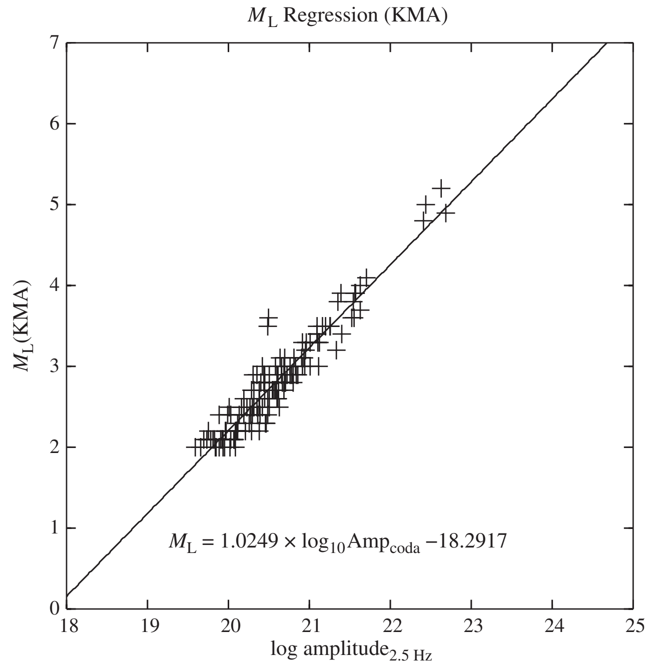

Figure 6. Results of M_L regression for KMA using the amplitudes of derived source spectra at the 2–3-Hz band.

For E_R computation, we assumed that the contribution of the P wave (E_P) was 7% of E_S (Mayeda and Walter, 1996).

To investigate whether the earthquakes that occurred in this region follow self-similarity or not, we performed a self-similarity test (e.g., Yoo *et al.*, 2010) and derived scaling relationships between the estimated source parameters. We tested whether our dataset obeys self-similarity by using a grid-search method similar to that applied in $S(f)$ estimation. At this time, we used path-corrected amplitudes of all events with $M_w > 2.0$ and coda-derived moment magnitudes to find the best apparent stress and scaling parameter. The results were quite different from the grid-search results for relatively large events (Fig. 4a). Figure 4b clearly shows nonself-similarity with a nonzero scaling parameter of $\varepsilon = 0.53$ (see Fig. 4b). This indicates that our observations cannot be explained by self-similar scaling over a broad range of moments.

We also derived three scaling relationships: f_c versus M_0, E_R versus M_0, and $\tilde{e}$ versus M_0, where $\tilde{e}$ indicates the scaled energy defined by E_R/M_0. If the earthquakes obey self-similarity, the relation between f_c and M_0 should be $M_0 \propto f_c^{-3}$ (Kanamori and Anderson, 1975). However, the relation needs to be modified to consider nonself-similarity and $M_0 \propto f_c^{-(3+\varepsilon)}$ was suggested by Kanamori and Rivera (2004). The scaled energy can be interpreted as a measure of seismic efficiency, which indicates the radiated energy per unit area and per unit slip on the fault plane. For earthquakes with the same seismic moments, higher scaled energy indicates the earthquake has a higher corner frequency and radiates more high-frequency energy than the earthquake with lower scaled energy. Under the self-similarity assumption, the scaled energy and apparent stress ($\sigma_a = \mu\tilde{e}$, where

μ is rigidity) are constant and size independent because the radiated energy is simply proportional to seismic moment (or total slip), while those parameters are not constant for nonself-similarity.

Figure 7 shows the relationship between seismic moments and their corresponding corner frequencies. The overall trend is clearly different from the trends theoretically calculated under the self-similarity assumption for various apparent stresses (Fig. 7). The scaling parameter ε was determined by finding the best-fitting line. Because we have only a few data points for large earthquakes ($M_w > 5.0$), the traditional least-square inversion reflects the trend for small earthquakes. To reduce this effect, we provided a constraint where the fitting line must pass the point for the largest event. The estimated scaling parameter was 0.54, and this value is quite similar with the previous value obtained from the self-similarity test (see Fig. 4b). Although the overall trend can be explained by the simple linear relation, there appears to be a stepwise change in apparent stress at $M_w \sim 5.0$. The apparent stress is larger and more or less constant for larger events ($M_w > 5.0$), but it becomes smaller for smaller events ($M_w < 5.0$). This observation is consistent with previous studies for Chi-Chi in Taiwan (Mayeda and Malagnini, 2009) and Wells in Nevada (Mayeda and Malagnini, 2010).

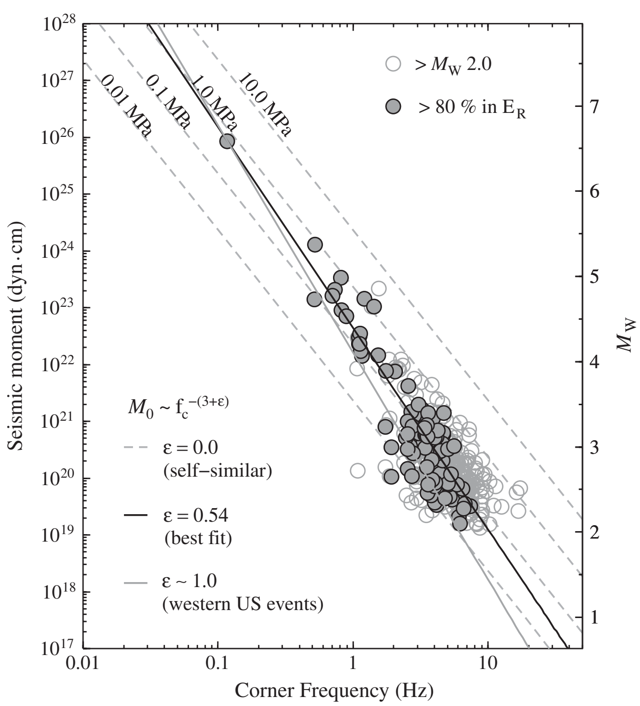

Figure 7. Corner frequency versus seismic moment for the earthquakes with $M_w > 2.0$ (Gray open circles). The dark solid circles indicate the selected events, radiated energies of which are calculated without corrections for band limitation to be larger than 80% of the corrected radiated energies. The black line indicates the best-fit regression using all events with $M_w > 2.0$. The gray line indicates the same regression line for events in the western United States (Mayeda and Walter, 1996). For reference, the plots of the self-similar scaling lines for constant apparent stresses of 0.01, 0.1, 1, and 10 MPa are shown with dotted gray lines.

The scaling relation of the radiated energy versus seismic moment also shows that the earthquakes are likely to follow nonself-similarity (Fig. 8a). Because our radiated energy calculation can be biased when the observations cover a narrow frequency range, we calculated the ratio (λ) of the radiated energy with and without a limited frequency correction. We selected only events with $\lambda > 0.8$. This indicates that the effect due to the limited frequency band is small. The scaling relation derived from only the selected events was consistent with that for all of the events. This confirms that the limited frequency band does not distort the result. The trend of the radiated energy versus seismic moment shows that the increasing rate of radiated energy with increasing seismic moment changes at a seismic moment of about 10^{21} dyn·cm (Fig. 8a). This observation is more or less consistent with previous results obtained from different datasets and methodologies (e.g., Abercrombie, 1995; Mayeda and Walter, 1996; Kanamori and Heaton, 2000). The scaling relation of the scaled energy versus seismic moments represents this feature more clearly (Fig. 8b). The scaling relation of the scaled energy versus moment magnitude in the 2005 Fukuoka sequence was studied by Yoo *et al.* (2010) using the coda waves recorded at regional distances with good azimuthal coverage. They reported that the scaled energy gradually increases between M_w 4.0 and 5.0 and becomes more or less constant at $M_w > 5.0$. However, the trend of the scaled energy at smaller magnitudes is not well constrained due to the lower limit of the magnitude (M_w 3.4). Our dataset includes 12 events that belong to the 2005 Fukuoka sequence. Although we used stations with large epicentral distances, and their azimuthal coverage is not as good as the previous study (Yoo *et al.*, 2010), scaling of the scaled energy for those 12 events showed a consistent trend with the previous estimate of the scaling relation for the sequence (Fig. 8b). This indicates that our measurements are reliable. Many small events analyzed in this study resulted in the scaled energy scaling for a broad range of magnitudes ($2.0 < M_w < 6.6$). Our results show that the scaled energy rapidly increases from a seismic moment of 10^{19} to about 10^{21} dyn·cm, but the increasing rate becomes small for events with M_0 larger than 10^{21} dyn·cm ($M_w \sim 3.3$). Because the scaled energy is proportional to the radiated seismic energy per unit slip and unit fault area, our observation indicates that the efficiency of the energy radiation through seismic waves is size dependent and varies greatly at lower magnitudes ($M_w < 3.3$). The change in nonself-similarity for small and large earthquakes has been reported by previous studies (e.g., Abercrombie, 1995; Mayeda and Walter, 1996; Morasca *et al.*, 2005) for different regions and datasets and can be explained by the difference in rupture dynamics for small and large earthquakes (e.g., Kanamori and Heaton, 2000; Brodsky and Kanamori, 2001).

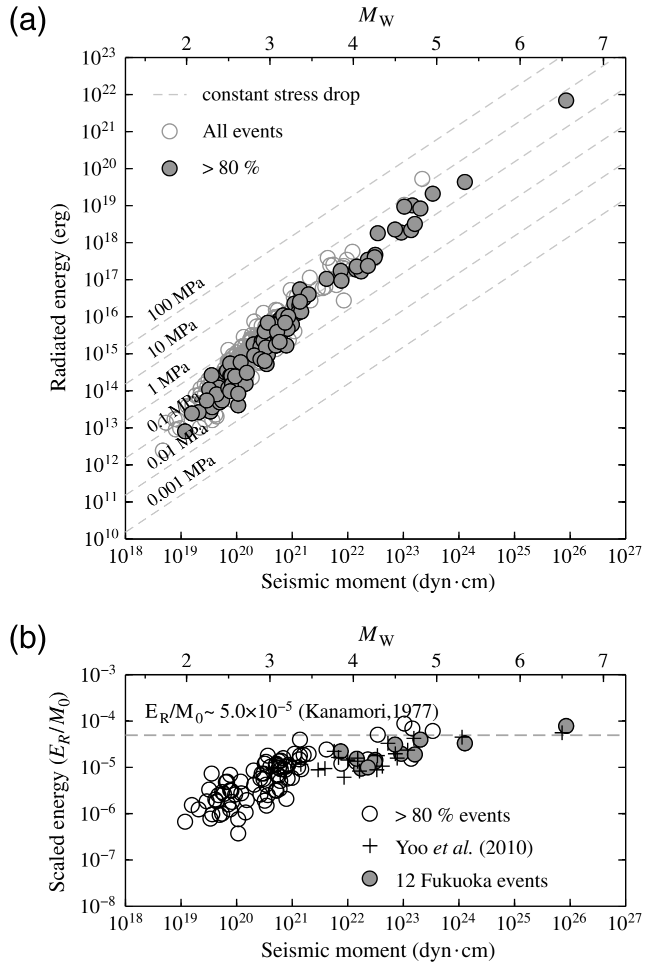

Figure 8. (a) Radiated energy and seismic moment for the earthquakes with $M_w > 2.0$ (open circles). Dark solid circles represent the same plot for selected events, radiated energies of which are calculated without corrections for band limitation to be larger than 80% of the corrected radiated energies. Dotted gray lines indicate the self-similar scaling lines for constant stress drop of 0.001, 0.1, 1, 10, 100 MPa. (b) Scaled energy versus seismic moment for the events. The open black circles indicate selected events (dark solid circle in [a]). Crosses and dark solid circles indicate 20 Fukuoka events from Yoo *et al.* (2010) and 12 common events in our study. The dotted gray line represents constant scaled energy obtained from large earthquakes (~5.0×10^{-5}; Kanamori, 1977).

Conclusion

We successfully transported the coda source spectrum method to earthquakes that occurred in and around the Korean Peninsula. Stable source spectra were derived from coda waves after careful corrections for path and site effects. From the derived source spectrum, we measured the seismic moment, local magnitude, corner frequency, radiated energy, and scaled energy. The complete M_w catalog of the earthquakes for 2001–2007 was reported for the first time, and continuous measurements of M_w for future earthquakes can be used to investigate earthquake characteristics and potential seismic hazards in the region.

The scaling relations of the corner frequency, radiated energy, and scaled energy, versus the seismic moment, clearly indicate that the earthquakes follow nonself-similarity. The scaled energy scaling indicates that large earthquakes radiate seismic energy more efficiently than small ones. Moreover, we found a clear change in the trend of scaled energy versus seismic moment for small and large earthquakes. This observation is more or less consistent with previous results for different regions and implies that the rupture dynamics of small and large earthquakes are different. Although many more studies are necessary to reach a consensus, our result supports the nonself-similarity of earthquakes.

Data and Resources

Seismograms used in this study were collected using the networks of Korea Institute of Geoscience and Mineral Resources (KIGAM) and Korea Meteorological Administratio (KMA). KIGAM and KMA data can be obtained from the web page at http://quake.kigam.re.kr and http://kma.go.kr, respectively (last accessed 9 March 2011). However, permission is required to access the KIGAM data center.

For the site correction used in this paper, predefined seismic moments were obtained in part from the F-net moment tensor catalog (http://www.f-net.bosai.go.jp, last accessed May 2011).

Acknowledgments

We thank the operators of the Korea Institute of Geoscience and Mineral Resources and the Korea Meteorological Administration for making their data publicly available. We thank Eric Chael and two anonymous reviewers for helpful comments. This work was funded by the Korea Meteorological Administration and Development Program under Grant CATER 2008-5113. K. Mayeda was supported under Weston Geophysical subcontract GC19762NGD and AFRL contract FA8718-09-C-0014.

References

Abercrombie, R. E. (1995). Earthquake source scaling relationships from −1 to 5 M_L using seismograms recorded at 2.5-km depth, *J. Geophys. Res.* **100,** 24015–24036.

Aki, K. (1969). Analysis of the seismic coda of local earthquakes as scattered waves, *J. Geophys. Res.* **74,** 615–631.

Aki, K., and B. Chouet (1975). Origin of coda waves: Source, attenuation and scattering effects, *J. Geophys. Res.* **80,** 3322–3342.

Brodsky, E. E., and H. Kanamori (2001). Elastohydrodynamic lubrication of faults, *J. Geophys. Res.* **106,** 16,357–16,374.

Brune, J. N. (1970). Tectonic stress and the spectra of seismic shear waves from earthquakes, *J. Geophys. Res.* **75,** 4997–5009

Choy, G. L., and J. L. Boatwright (1995). Global patterns of radiated seismic energy and apparent stress, *J. Geophys. Res.* **100,** 18,205–18,228.

Ford, S. R., D. S. Dreger, K. Mayeda, W. R. Walter, L. Malagnini, and W. S. Phillips (2008). Regional attenuation in northern California: A comparison of five 1D *Q* methods, *Bull. Seismol. Soc. Am.* **98,** 2033–2046.

Hanks, T. C., and H. Kanamori (1979). A moment magnitude scale, *J. Geophys. Res.* **84,** 2348–2350.

Ide, S., and G. C. Beroza (2001). Does apparent stress vary with earthquake size?, *Geophys. Res. Lett.* **28,** 3349–3352.

Ide, S., G. C. Beroza, S. G. Prejean, and W. L. Ellsworth (2003). Apparent break in earthquake scaling due to path and site effects on deep borehole recordings, *J. Geophys. Res.* **108**, no. 2271, doi 10.1029/2001JB001617.

Izutani, Y. (2005). Radiated energy from the mid Niigata, Japan, earthquake of October 23, 2004, and its aftershocks, *Geophys. Res. Lett.* **32,** L21313, doi 10.1029/2005GL024116.

Izutani, Y., and H. Kanamori (2001). Scale-dependence of seismic energy-to-moment ratio for strike-slip earthquakes in Japan, *Geophys. Res. Lett.* **28,** 4007–4010.

Kanamori, H. (1977). The energy release in great earthquakes, *J. Geophys. Res.* **82,** 2981–2987.

Kanamori, H., and D. L. Anderson (1975). Theoretical basis of some empirical relations in seismology, *Bull. Seismol. Soc. Am.* **65,** 1073–1095.

Kanamori, H., and T. H. Heaton (2000). Microscopic and macroscopic physics of earthquakes, in *Geocomplexity and the Physics of Earthquakes*, J. B. Rundle, D. Turcotte, and W. Klein (Editors), American Geophysical Monograph 120, 147–163.

Kanamori, H., and L. Rivera (2004). Static and dynamic scaling relations for earthquakes and their implications for rupture speed and stress drop, *Bull. Seismol. Soc. Am.* **94,** 314–319.

Kanamori, H., J. Mori, E. Hauksson, T. H. Heaton, L. K. Hutton, and L. M. Jones (1993). Determination of earthquake energy release and M_L using TERRASCOPE, *Bull. Seismol Soc Am.* **83,** 330–346.

Malagnini, L., A. Akinci, R. B. Herrmann, N. A. Pino, and L. Scognamiglio (2002). Characteristics of the ground motion in northeastern Italy, *Bull. Seismol. Soc Am.* **92,** 2186–2204.

Malagnini, L., K. Mayeda, A. Akinci, and P. L. Bragato (2004). Estimating absolute site effects, *Bull. Seismol. Soc Am.* **94,** 1343–1352.

Mayeda, K., and L. Malagnini (2009). Apparent stress and corner frequency variations in the 1999 Taiwan (Chi-Chi) sequence: Evidence for a step-wise increase at $M_w \sim 5.5$, *Geophys. Res. Lett.* **36,** L10308, doi 10.1029/2009GL037421.

Mayeda, K., and W. R. Walter (1996). Moment, energy, stress drop, and source spectra of western United States earthquakes from regional coda envelopes, *J. Geophys. Res.* **101,** 11,195–11,208.

Mayeda, K., and L. Malagnini (2010). Source radiation invariant property of local and near-regional shear-wave coda: Application to source scaling for the M_w 5.9 Wells, Nevada sequence, *Geophys. Res. Lett.* **37,** L07306, doi 10.1029/2009GL042148.

Mayeda, K., R. Gök, W. R. Walter, and A. Hofstetter (2005). Evidence for non-constant energy/moment scaling from coda-derived source spectra, *Geophys. Res. Lett.* **32,** L10306, doi 10.1029/2005GL022405.

Mayeda, K., A. Hofstetter, J. L. O'Boyle, and W. R. Walter (2003). Stable and transportable regional magnitudes based on coda-derived moment-rate spectra, *Bull. Seismol. Soc. Am.* **93,** 224–239.

Mayeda, K., L. Malagnini, and W. R. Walter (2007). A new spectral ratio method using narrow band coda envelopes: Evidence for non-self-similarity in the Hector Mine sequence, *Geophys. Res. Lett.* **34,** L11303, doi 10.1029/2007GL030041.

McGarr, A. (1999). On relating apparent stress to the stress causing earthquake fault slip, *J. Geophys. Res.* **104,** 3003–3011.

Morasca, P., K. Mayeda, L. Malagnini, and W. R. Walter (2005). Coda-derived source spectra, moment magnitudes and energy-moment scaling in the western Alps, *Geophys. J. Int.* **160,** 263–275.

Morasca, P., K. Mayeda, R. Gok, W. S. Phillips, and L. Malagnini (2008). 2D coda and direct-wave attenuation tomography in northern Italy, *Bull. Seismol. Soc. Am.* **98,** 1936–1946, doi 10.1785/0120070089.

Murphy, K. R., K. Mayeda, and W. R. Walter (2009). *Lg*-coda methods applied to Nevada Test Site events: Spectral peaking and yield estimation, *Bull. Seismol Soc Am.* **99,** 441–448.

Powell, M. D. J. (1964). An efficient method for finding the minimum of a function of several variables without calculation derivatives, *Comput. J.* **7,** 155–162.

Prieto, G. A., P. M. Shearer, F. L. Vernon, and D. Kilb (2004). Earthquake source scaling and self-similarity estimation from stacking *P* and *S* spectra, *J. Geophys. Res.* **109,** no. B08310, doi 10.1029/2004JB003084.

Rautian, T. G., and V. I. Khalturin (1978). The use of the coda for determination of the earthquake source spectrum, *Bull. Seismol. Soc. Am.* **68,** 923–948.

Rhie, J., and S. Kim (2010). Regional moment tensor determination in the southern Korean Peninsula, *Geoscience J.* **14,** 329–333.

Singh, S. K., and M. Ordaz (1994). Seismic energy release in Mexican subduction zone earthquakes, *Bull. Seismol. Soc. Am.* **84,** 1533–1550.

Street, R. L., R. B. Herrmann, and O. W. Nuttli (1975). Spectral characteristics of the *Lg* wave generated by central United States earthquakes, *Geophys. J. Roy. Astron. Soc.* **41,** 51–63.

Taylor, S. R., A. A. Velasco, H. E. Hartse, W. S. Phillips, and R. Walter (2002). Amplitude corrections for regional seismic discriminants, *Pure Appl. Geophys.* **159,** 623–650.

Venkataraman, A., G. C. Beroza, S. Ide, K. Imanishi, H. Ito, and Y. Iio (2006). Measurements of spectral similarity for microearthquakes in western Nagano, Japan, *J. Geophys. Res.* **111,** no. B03303, doi 10.1029/2005JB003834.

Walter, W. R., and S. R. Taylor (2001). A revised magnitude and distance amplitude correction (MDAC2) procedure for regional seismic discriminants: Theory and testing at NTS, Report UCRL-ID-146882, Lawrence Livermore National Laboratory, Livermore, California, available at http://www.llnl.gov/tid/lof/documents/pdf/240563.pdf (last accessed May 2011).

Yoo, S.-H., J. Rhie, H.-S. Choi, and K. Mayeda (2010). Evidence for non-self-similarity and transitional increment of scaled energy in the 2005 west off Fukuoka seismic sequence, *J. Geophys. Res.* **115,** no. B08308, doi 10.1029/2009JB007169.

Zolezzi, F., P. Morasca, K. Mayeda, W. S. Phillips, and C. Eva (2008). Attenuation tomography of the southern Apennines (Italy), *J. Seismol.* **12,** 355–365, doi 10.1007/s10950-007-9079-6.

School of Earth and Environmental Sciences
Seoul National University
1 Gwanak-ro
Gwanak-gu
Seoul 151-742
South Korea
rhie@snu.ac.kr
(S.-H.Y., J.R.)

Korea Institute of Nuclear Safety (KINS)
34 Gwahak-ro
Yuseong-gu
Daejeon 305-338
South Korea
(H.C.)

Berkeley Seismological Laboratory
215 McCone Hall
University of California, Berkeley
Berkeley, California 94720-4760
(K.M.)

Manuscript received 17 November 2010